Nano Research 2018, 11(8): 4323–4332
https://doi.org/10.1007/s12274-018-2020-1
Research Article
ISSN 1998-0124
CN 11-5974/O4

Insights into the efficiency and stability of Cu-based nanowires for electrocatalytic oxygen evolution

Jun Yu[1], Qi Cao[1], Bin Feng[2], Changli Li[3], Jingyuan Liu[4], J. Kenji Clark[1], and Jean-Jacques Delaunay[1] (✉)

[1] *Department of Mechanical Engineering, The University of Tokyo, 7-3-1 Hongo, Bunkyo-ku, Tokyo 113-8656, Japan*
[2] *Institute of Engineering Innovation, The University of Tokyo, 7-3-1 Hongo, Bunkyo-ku, Tokyo 113-8656, Japan*
[3] *School of Materials Science and Engineering, Tsinghua University, Beijing 100084, China*
[4] *Department of Chemical System Engineering, The University of Tokyo, 7-3-1 Hongo, Bunkyo-ku, Tokyo 113-8656, Japan*

Received: 25 September 2017
Revised: 31 January 2018
Accepted: 11 February 2018

KEYWORDS
oxygen evolution reaction,
crystalline CuO,
active phase,
copper ion diffusion

ABSTRACT

Copper oxide nanowires with varying oxidation states are prepared and their activity for water oxidation is studied. The nanowires with a CuO phase are found to be the most active, and their degree of crystallinity is important in achieving efficient water oxidation. For the crystalline CuO nanowires in a weakly basic Na_2CO_3 electrolyte, a Tafel slope of 41 mV/decade, an overpotential of approximately 500 mV at ~ 10 mA/cm^2 (without compensation for the solution resistance), and a faradaic efficiency of nearly 100% are obtained. This electrode maintains a stable current for over 15 h. The low overpotential of 500 mV at 10 mA/cm^2, small Tafel slope, long-term stability, and low cost make CuO one of the most promising catalysts for water oxidation. Moreover, the evolution of the CuO nanowire morphology over time is studied by electron microscopy, revealing that the diffusion of Cu ions from the interior of the nanowires to their surface causes the aggregation of individual nanowires over time. However, despite this aggregation, the current density remains nearly constant, because the total electrochemically active surface area of CuO does not change.

1 Introduction

A wide range of environmental problems, such as acid rain and the greenhouse effect, are exacerbated by the ongoing use of fossil fuels [1–4]. Water splitting is regarded as a potential way to produce hydrogen energy, which is an alternative to fossil fuels. The demand for clean and sustainable energy has inspired researchers to focus on the water splitting technology. The oxygen evolution reaction (OER) is a crucial step in the water splitting reaction because of its more complex and sluggish reaction dynamics [5–9]. For many years, researchers have been endeavoring to find suitable anode materials for the OER. An ideal anode material should have a small overpotential, have a high efficiency, be abundant in the earth, and most importantly have long-term stability [10, 11]. Until now, Co- [12–16] and Ni- [17–19] based electrodes have been studied broadly for use in the OER because of their high activity and good stability. However, the high performance is

Address correspondence to jean@mech.t.u-tokyo.ac.jp

usually achieved in combination with other materials or by using substrates with large surface areas. This increases the complexity of the fabrication of the electrodes, and their costs.

Cu-based catalysts [20–26] have been widely used to solve environmental and energy-related problems. In particular, Cu_2O has been widely studied as a potential low-cost catalyst for solar H_2 generation [27–29]. The first time a copper-based catalyst was applied to electrolytic water oxidation was in 2012, when a copper-bipyridine catalyst was reported [30]. Following this, the role of Cu(II) ions in water oxidation was investigated thoroughly [10, 31], and it was shown that water can be oxidized by Cu(II) ions dissolved in weakly basic electrolytes [31]. Anodic corrosion of the copper electrode could be prevented by the formation of a compact film directly from the Cu(II) in the electrolyte. However, the improved performance required the addition of Cu(II) ions into the electrolyte [10, 32]. To solve this problem, copper oxide (Cu-Bi thin film) was synthesized and used for water oxidation. This catalyst sustained a steady current density of 1.2 mA/cm^2 (overpotential η = 660 mV) for 11 h [32] and did not require the addition of extra Cu(II) ions. However, the relatively low current density and high overpotential of the catalyst are unsatisfactory. The poor water oxidation performance of these Cu-based catalysts may be caused by a lack of the active species in the Cu-based catalysts. Recently, $Cu(OH)_2$ was reported to be active for the OER in a 0.1 M NaOH electrolyte [33]. However, the $Cu(OH)_2$ material is not stable in a high pH solution and the morphology of the electrode after the stability test was not displayed in the report. A solid understanding of the behavior of Cu-based materials during the OER process remains elusive: it is unclear which phase is the dominant active phase in Cu-based catalysts and what governs the stability of Cu-based catalysts.

In this work, the OER activities of $Cu(OH)_2$, Cu_2O, Cu_xO, and CuO nanowires with varying degrees of crystallinity are investigated. CuO is found to be the active phase for the OER, and increasing crystallinity could improve the catalytic activity. A sample with highly crystalline CuO nanowires achieves the best performance with a Tafel slope of 41 mV/decade, an overpotential (η) of ~ 500 mV at ~ 10 mA/cm^2 (without compensation for the solution resistance), and nearly 100% faradaic efficiency in a weakly basic Na_2CO_3 solution (pH 10.8). Moreover, the current density of the electrode remains constant at ~ 10 mA/cm^2 for more than 15 h. The evolution of the chemical states and morphological structure of the CuO electrode during and after the stability test is revealed and discussed, providing direct evidence of the stability of the CuO electrode. To the best of our knowledge, the CuO nanowires catalyst reported here has one of the best performances reported so far among OER catalysts in weakly basic electrolytes.

2 Experimental

2.1 Synthesis of $Cu(OH)_2$ nanowires

$Cu(OH)_2$ nanowires were directly grown from a copper foil using a simple wet chemistry method [34]. First, the copper foil (99.6%, Nilaco) with a size of 10 mm × 10 mm and a thickness of 0.2 mm was cleaned in an ultrasonic bath for 5 min with acetone first and then ethanol. The foil was then rinsed three times with deionized water. Afterwards, the cleaned copper foil was treated by submersion in a mixture of 2.67 M NaOH (97.0%, Wako) and 0.133 M $(NH_4)_2S_2O_8$ (98.0%, Wako) kept at 5 ˚C for 15 min. Finally, the copper foil, showing a blue color, was picked up from the solution, washed by deionized water, and dried in air.

2.2 Synthesis of Cu_xO nanowire layers

Cu_xO nanowire layers were synthesized from as-prepared $Cu(OH)_2$ nanowires via a two-step annealing process. $Cu(OH)_2$ nanowire layers were thermally treated at 120 ˚C for 2 h and subsequently heated in air to 150, 180, 210, or 250 ˚C for 3 h at a rate of 5 ˚C/min. The samples were named according to the annealing temperature used in the second step (i.e., the A-150, A-180, A-210, and A-250 samples).

2.3 Structural characterization

Scanning electron microscope (SEM) images were obtained from a field-emission SEM (JEOL JSM 7600 FA, Japan). Grazing incidence X-ray diffraction (XRD) patterns were recorded on an X-ray diffractometer (SmartLab, Rigaku Co. Ltd, Japan) with Cu Kα radiation (incident angle = 0.5°, λ = 1.541 Å, step size = 0.02°, dwelling time = 2 s). Raman spectra were collected on

a Renishaw inVia™ Raman Microscope system with a 488 nm excitation laser (0.82 mW) directed through a 100 × objective at room temperature. X-ray photoelectron spectroscopy (XPS) studies were carried out on a PHI 5000 VersaProbe (ULVAC-PHI) with an Al-Kα X-ray source (1,486.6 eV). The electron analyzer was operated at pass energies of 117.4 eV for the wide scans and 23.5 eV for the narrow scans. Transmission electron microscopy (TEM) and high-angle annular dark-field (HAADF)-scanning transmission electron microscopy (STEM) observations were carried out with a JEM-2010 TEM (JEOL Co. Ltd., Japan) and an ARM-200CF TEM (JEOL Co. Ltd., Japan) each operated at 200 kV. The HAAD-STEM observations were acquired with a probe-forming aperture semi-angle of 22 mrad and a detection angle of 90–370 mrad.

2.4 Electrochemical measurements

The electrochemical measurements were conducted in a cylindrical glass cell with a typical three-electrode configuration. The fabricated nanowire electrodes were used as the working electrode, and the reference electrode and counter electrode were an Ag/AgCl electrode and a Pt wire, respectively. The applied potential of the working electrode was controlled using a potentiostat (VersaSTAT 4, Princeton Applied Research). The potentials vs. the Ag/AgCl reference electrode were converted to the reversible hydrogen electrode (RHE) scale using Nernst's equation

$$E_{RHE} = E_{Ag/AgCl} + 0.059\ pH + E^{0}_{Ag/AgCl} \quad (1)$$

where $E_{Ag/AgCl}$ is the measured potential against the reference electrode and $E^{0}_{Ag/AgCl}$ = 0.1976 V at 25 °C. The current density (J)–potential (V) curves and Tafel plots were obtained using controlled potential electrolysis in 1 M Na_2CO_3 (pH 10.8), with a scan rate of 50 mV/s for the J–V curve and a scan rate of 1 mV/s for the Tafel plot. Prior to each experiment, the electrolyte was stirred and purged with N_2 gas for 20 min. N_2 purging was continued throughout the electrochemical measurements. The iR drop of the Tafel plots were corrected for the solution resistance, which was determined using the electrochemical impendence spectroscopy (EIS) technique [8]. EIS measurements were conducted in the same configuration as the other electrochemical measurements and under the potential corresponding to the current density of 10 mA/cm^2, with the frequency ranging from 100 kHz to 1 Hz. Unless otherwise stated, all the potentials were reported vs. RHE without iR compensation and all experiments were performed at room temperature. An on-line micro-gas chromatograph (GC-3000A, Agilent) was used to record the amounts of generated O_2 and H_2 during the water oxidation reaction. The faradaic efficiency was calculated according to the ratio of the number of electrons in the detected oxygen/hydrogen molecules to the number of electrons injected by the current.

3 Results and discussion

Through a wet chemistry process, as described in the experimental section and depicted in Fig. 1(a), we prepared $Cu(OH)_2$ nanowires (Fig. 1(b)) from copper foil. The diameters of the $Cu(OH)_2$ nanowires were as small as 56 nm. After annealing the $Cu(OH)_2$ samples at 180 °C (i.e., the A-180 sample) and 250 °C (i.e., the A-250 sample), both samples still had a dense-nanowire morphology, although a slight increase in the diameter of the nanowires with increased annealing temperature was observed.

The crystal structures of the various nanowires were examined by XRD, and the spectra are shown in Fig. 2(a). For the $Cu(OH)_2$ nanowires, several strong peaks associated with copper hydroxide (JCPDS 13-0420) could be identified. Two additional small peaks that could be attributed to the copper substrate (JCPDS 04-0836) were also seen. After annealing, the copper hydroxide peaks disappeared. For the sample annealed at 150 °C, low-intensity peaks ascribed to CuO (JCPDS 65-2309) were detected. For the samples annealed at 180 °C or higher, the intensity of the CuO peaks was much stronger. The main peaks could be indexed to the ($\bar{1}11$), (111), ($\bar{1}13$), ($\bar{2}02$), and (110) planes of CuO. For the samples annealed at 210 and 250 °C, additional peaks associated with the Cu_2O phase (JCPDS 65-3288) were detected. This suggests that, upon annealing, the $Cu(OH)_2$ sample transforms first to CuO at moderate annealing temperatures, and then to a mixture of CuO and Cu_2O at higher temperatures.

The Raman spectra of the different samples are displayed in Fig. 2(b). CuO has a C^{6}_{2h} space group structure and each primitive cell contains two molecules. Among the nine zone-center optical phonon modes

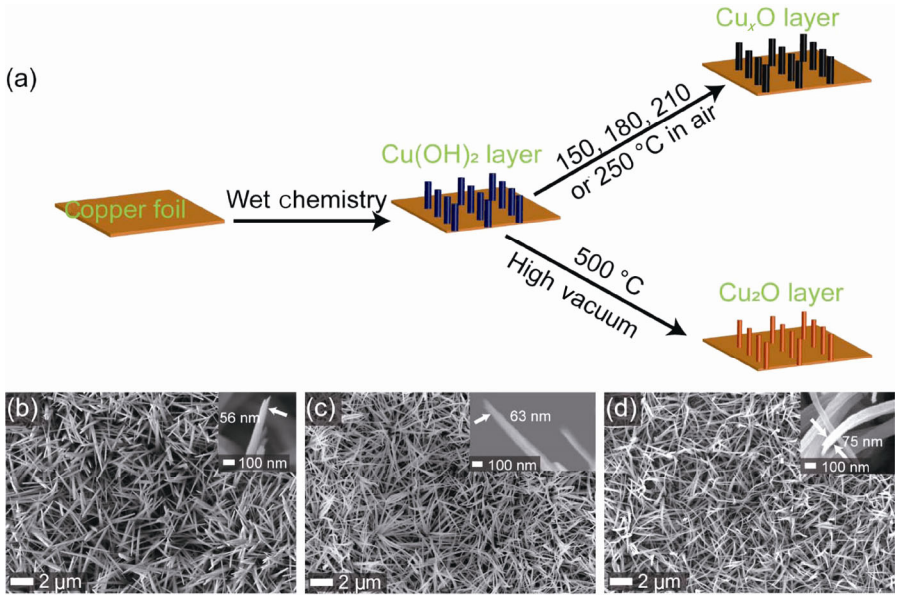

Figure 1 (a) Schematic illustration of the synthesis procedures for the Cu_xO nanowire layers; SEM images of the $Cu(OH)_2$ (b), A-180 (c), and A-250 samples (d), with insets revealing the nanowires under higher magnifications.

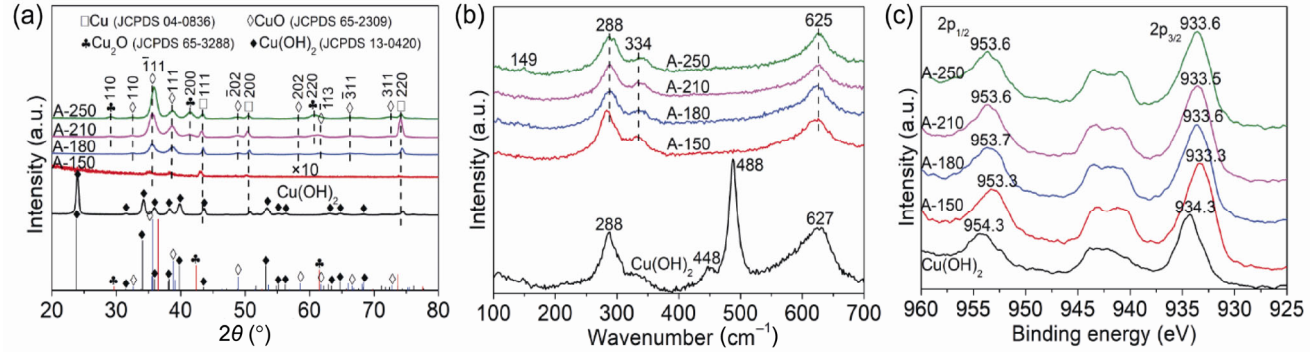

Figure 2 (a) X-ray diffraction patterns, (b) Raman spectra, and (c) XPS spectra of the obtained $Cu(OH)_2$, as well as the A-150, A-180, A-210, and A-250 samples.

with symmetries $3A_u + 3B_u + A_g + 2B_g$ [35], there are three Raman active modes ($A_g + 2B_g$) [36] for CuO. According to results in the literature [36, 37], we can assign the peak at 288 cm^{-1} to the A_g mode and the peaks at 334 and 625 cm^{-1} to the B_g modes. For all samples except for the $Cu(OH)_2$ and A-250 sample, only CuO vibrational modes were observed. For the A-250 sample, an extra peak at 149 cm^{-1} related to the intrinsic Γ_{15}^- IR active modes of the Cu_2O phase [37, 38] was observed. This suggests that in addition to CuO, Cu_2O was also formed in the sample annealed at 250 ˚C.

The surface states of the samples were analyzed using XPS. Figure 2(c) shows the XPS spectra of the samples. A set of peaks including the Cu $2p_{3/2}$ peak (934.3 eV) and the Cu $2p_{1/2}$ peak (954.3 eV) were observed. Meanwhile, additional intense satellite peaks of Cu(II) were also observed [39]. These peaks are ascribed to the standard peaks of $Cu(OH)_2$. For those samples obtained after annealing, in addition to the intense satellite peaks ascribed to the binding energies of CuO, the Cu $2p_{3/2}$ and $2p_{1/2}$ peaks were identified to be at 933.3–933.6 eV and 953.3–953.7 eV, respectively [10, 39].

In the transformation of copper hydroxide to copper oxide, the annealing temperature plays a key role. Annealing at 150 ˚C for 3 h was insufficient for the formation of highly crystalline copper oxide, as evidenced by the XRD results (Fig. 2(a)). When the annealing temperature was increased to 180 ˚C, CuO with a high degree of crystallinity was formed. An additional Cu_2O phase was observed for the samples annealed at a

temperature higher than 210 ˚C. Previous reports have revealed that under an oxygen-moderate environment and a high annealing temperature, a Cu_2O mid-layer can form from the oxidization of the copper substrate and the removal of oxygen from the CuO lattice [29, 40]. This may be the reason why Cu_2O was detected by XRD on the samples annealed at higher temperatures (Fig. 2(a)). In contrast to XRD, only peaks ascribed to CuO were detected by XPS. As XPS is a surface characterization technique, only the surface CuO was detected, and therefore the Cu_2O mid layer is not detected. For Raman spectroscopy, since the probing depth of the Raman laser is between that of XRD and XPS, a weak Cu_2O signal could be detected for the sample with the highest annealing temperature of 250 ˚C. In summary, an annealing temperature of 180 ˚C may be optimal to obtain nanowires with a pure CuO phase and high degree of crystallinity.

Cyclic voltammogram (CV) curves of the samples are shown in Fig. 3(a). The $Cu(OH)_2$ sample showed the lowest current density among all samples, with a maximum current density of 0.64 mA/cm^2 at a potential of 1.88 V. Upon annealing, the current density of all of the samples increased drastically. The A-180 sample exhibited the highest OER activity. The current density was 5 mA/cm^2 at 1.65 V (overpotential η = 0.42 V), 10 mA/cm^2 at 1.73 V (η = 0.5 V), and 37.64 mA/cm^2 at 1.88 V (η = 0.65 V). The current density of the A-150 sample was slightly lower, and the potentials required for 5 and 10 mA/cm^2 were 1.69 and 1.76 V, respectively. The current densities for the A-210 and A-250 samples were very similar, and required 1.79 and 1.80 V for 10 mA/cm^2, respectively. For the Cu_2O sample (Fig. S2 in the Electronic Supplementary Material (ESM)), the potential required for 10 mA/cm^2 was 1.86 V, which was higher than that of the A-210 and A-250 samples, indicating that the Cu_2O sample had the lowest OER activity among all of the samples.

In Fig. 3(b), the Tafel plots, OER current density as a function of the overpotential (log(i) vs. η), of the A-180, A-150, and A-210 samples are shown. The Tafel slopes for the A-180, A-150, and A-210 samples are 41, 49, and 66 mV/decade, respectively. The A-180 sample having the smallest Tafel slope of all samples is evidence for the superior OER activity of this sample, as a small Tafel slope indicates a catalyst is of good quality and has a high activity [41]. Mass transfer is favorable in catalysts with high-aspect-ratio morphologies and high crystallinities, because such structures reduce scattering losses during electron transfer [42, 43]. Smaller Tafel slopes generally indicate smaller internal barriers for electron and mass transport [32]. This may help to explain why the current density of the A-180 sample is larger than that of the A-150 sample. The formation of Cu_2O at high annealing temperatures leads to a decrease in the current density and an increase in the Tafel slope, demonstrating that CuO performs better as an electrode for OER. Moreover, the dense nanowire morphology could reduce the scattering loss during the electron transfer process and offer a large surface area for the active species to take part in the OER. Overall, the A-180 sample, with a large surface area and a highly crystalline CuO active phase, not only has the highest water-oxygen activity among our samples, but also boasts one of the best results ever reported for Cu-based OER catalysts [10, 30–32].

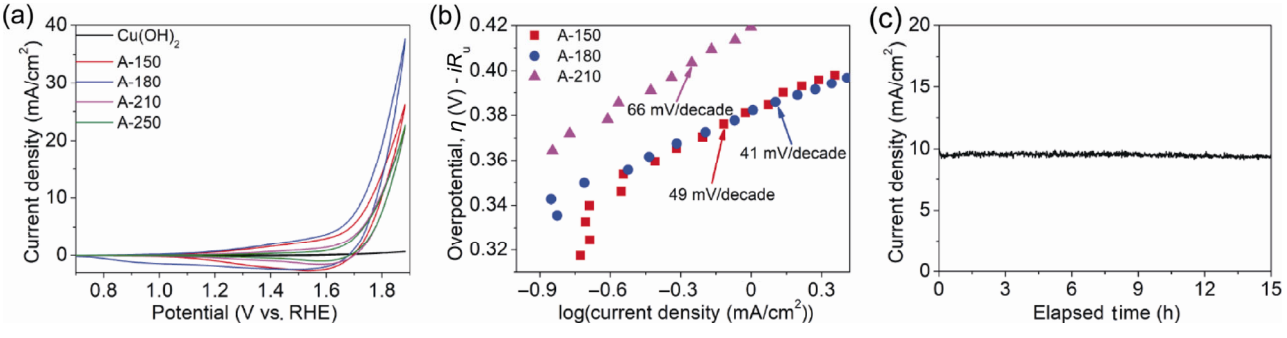

Figure 3 (a) CV curves of $Cu(OH)_2$, A-150, A-180, A-210, and A-250 samples for the OER without iR compensation with a scan rate of 50 mV/s. (b) Tafel plots collected from the steady-state CV measurement at a scan rate of 1 mV/s, which have been corrected for the iR drop of the solution. (c) Current density vs. time (J–t) curve of the A-180 sample obtained by fixing the electrolysis potential at 1.77 V vs. RHE without iR correction. The electrolyte was 1 M Na_2CO_3 (pH ≈ 10.8).

A controlled-potential water electrolysis test was done to verify the long-term performance and stability of the A-180 electrode, as shown in Fig. 3(c). With an applied potential of 1.77 V (η = 0.54 V), the current density remained nearly constant at 10 mA/cm^2 for more than 15 h. The small fluctuations in the current were attributed to the formation and detachment of O_2 bubbles on the electrode surface. The corresponding gas evolution was analyzed by on-line micro-gas chromatography, as shown in Fig. 4. For the 1-hour test, the amounts of hydrogen and oxygen gases produced were about 103.8 and 51.9 μmol, respectively, which correspond to a faradaic efficiency of nearly 100%. To investigate the stability of the electrode, SEM, Raman, and XPS characterizations of the A-180 electrodes were carried out after using the electrodes for 5, 10, 15, and 20 h in the water electrolysis reaction. The Raman results (Fig. 5(a)) showed that the vibrational peaks of CuO were preserved throughout the reaction [36, 37]. For the XPS results, shown in Fig. 5(b), the peak values of 933.1–933.6 eV for Cu $2p_{3/2}$ and 953.1–953.7 eV for Cu $2p_{1/2}$ were still consistent with the binding energies of CuO [10, 39]. Moreover, after a test of 20 h, as shown in Fig. S3 in the ESM, the A-180 electrode still had the optical appearance of CuO.

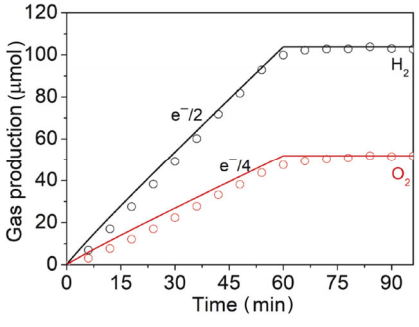

Figure 4 The time-dependent hydrogen and oxygen evolution for the A-180 electrode in a three-electrode configuration with an applied potential of 1.77 V vs. RHE without *iR* correction. The solid curves labelled $e^-/2$ and $e^-/4$ stand for the theoretical amount for hydrogen and oxygen evolution which are generated at 100% faradaic efficiency. The empty circles correspond to the recorded amount of hydrogen and oxygen gases detected during the measurement. The electrolyte was 1 M Na_2CO_3 (pH ≈ 10.8).

With increased electrolysis time, the morphology of the nanowires in the A-180 sample remained unchanged, as can be seen in Fig. 6. However, the nanowires tended to aggregate over time during the reaction (especially after 15 h), as confirmed by the magnified SEM images shown in the insets in Figs. 6(c) and 6(d). It is notable that after 20 h, nanosheet clumps were formed on some parts of the nanowire layer, as shown in Fig. 6(f). A Raman spectrum of the nanosheets is shown in Fig. S4 in the ESM. In addition to the CuO peaks described earlier, peaks at 699 and 1,385 cm^{-1} attributed to the ν_4 and ν_3 regions of CO_3^{2-} and two more peaks at 1,028 and 1,061 cm^{-1} attributed to the ν_1 symmetric stretching region of CO_3^{2-} were also found [44]. In this regard, it is speculated that CO_3^{2-} has been incorporated into the nanosheets and plays some role in their formation.

TEM and HAADF-STEM characterizations were exploited to further study the reason for the morphological change of the A-180 sample. Bright-field TEM images of a single nanowire before and after the 15-hour stability test are shown in Figs. 7(a) and 7(c). The selected-area electron diffraction (SAED) patterns (insets in Figs. 7(a) and 7(c)) display similar diffraction spots corresponding to the monoclinic CuO phase for the samples before and after the 15-hour reaction [45]. However, some dark spots appeared in Fig. 7(d), whereas the contrast in Fig. 7(b) was rather uniform. Since the intensity of the HAADF-STEM signal is sensitive to the sample thickness (if the atomic number of the materials is the same), a darker region suggests a smaller thickness. Given the dark regions are distributed mostly

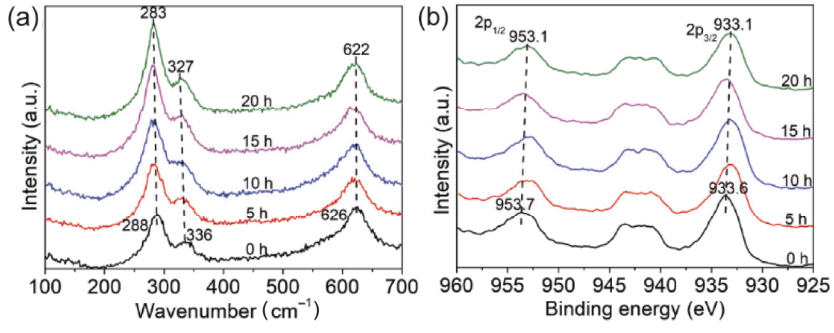

Figure 5 (a) Raman spectra and (b) XPS spectra of the A-180 sample after 0, 5, 10, 15, and 20 h of the stability tests.

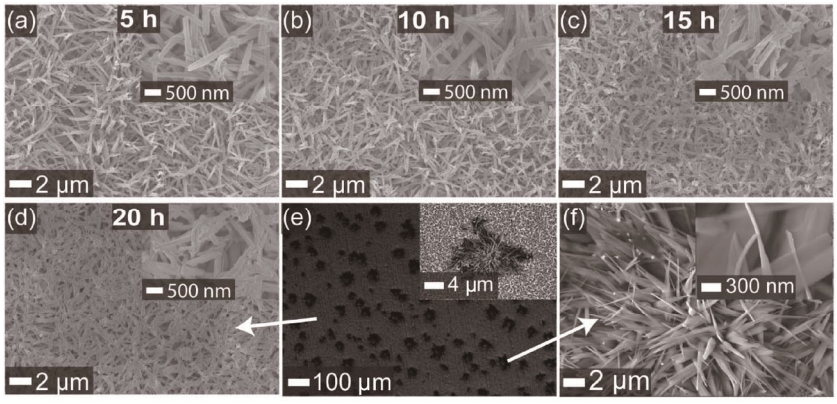

Figure 6 (a)–(c) SEM images of the A-180 sample after 5 h (a), 10 h (b), and 15 h (c) of the stability tests. (d)–(f) SEM images of the A-180 sample after 20 h of the stability test, with panel (e) showing the top-view morphology of the whole layer, and panels (d) and (f) showing the nanowire part and the clumps of nanosheets, respectively.

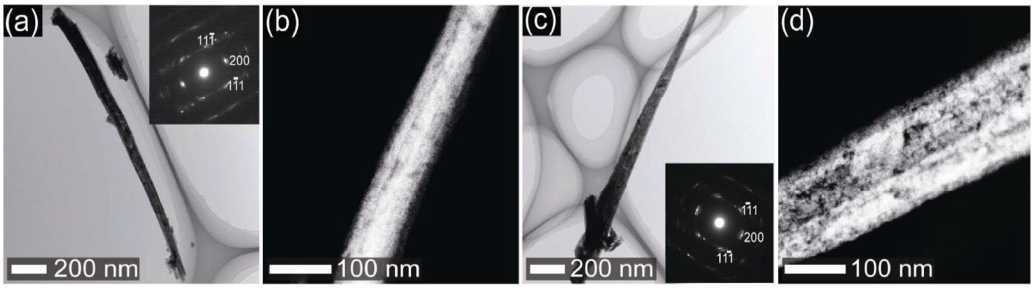

Figure 7 TEM images ((a) and (c)) and HAADF-STEM images ((b) and (d)) of the A-180 sample before ((a) and (b)) and after the 15-hour stability test ((c) and (d)). Insets of (a) and (c) are SAED patterns.

in the middle of the nanowires, as exhibited in Fig. 7(d), it is likely that after the 15-hour water electrolysis reaction, some inner copper ions diffused to the outside, resulting in a decreased density or the emergence of porosity in these CuO nanowires.

The electrochemical double-layer capacitance (C_{dl}) can be used to calculate the electrochemically active surface area (ECSA) according to Eq. (2)

$$\text{ECSA} = C_{dl}/C_s \quad (2)$$

where C_s is the constant related to the properties of the sample and its surface under identical electrolyte conditions [8, 46]. Figure 8 shows the EIS measurements of the A-180 sample before and after the 15-hour stability test (namely A-180-15 h). The calculated C_{dl} for the A-180 and A-180-15 h samples were 0.026 mF/cm^2 and 0.024 cm^{-2}, respectively, suggesting the ECSA of the A-180 CuO electrode was nearly unchanged after the stability test.

Based on the Raman and XPS results (Fig. 5), it is clear that even after the 15-hour reaction, the chemical

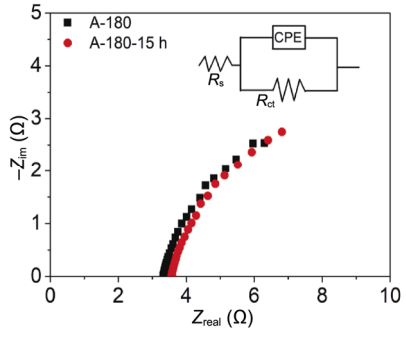

Figure 8 Nyquist plots of the A-180 sample before and after the 15-hour stability test. The inset shows the according equivalent circuit.

composition of the A-180 sample does not change, and it is still composed of CuO. With this understanding, it could be supposed that during the electrolysis reaction, copper ions have diffused from the interior to the surface of the nanowires, leading to an increase in the porosity and a decrease in the density of the nanowires. The diffused copper ions may fuse individual nanowires together, resulting in the aggregation of nanowires, as illustrated in Fig. 9 from panel (a) to

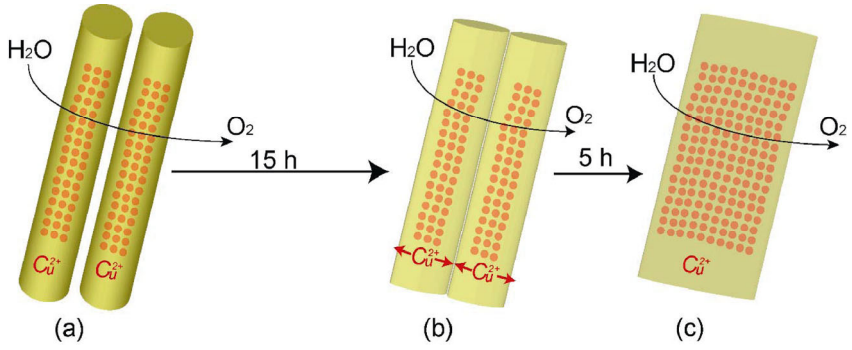

Figure 9 The morphological transformation process of CuO from nanowires to nanosheets during the reaction.

panel (b). The surface area of the active CuO species provided by the aggregated CuO nanowires is similar to the area provided by the non-aggregated nanowires, and therefore the current density remains stable despite the morphological change.

The reason for the formation of the nanosheets after 20 h of the stability test is still under investigation. We propose a possible explanation: The nanosheets were formed directly from the nanowires, as illustrated in Fig. 9. In the electrolysis process, copper ions diffuse from the interior to the surface of the nanowires and thus cause the aggregation of nanowires with decreased density (Figs. 9(a) and 9(b)). Afterwards, the aggregated CuO nanowires transform into nanosheets with the help of CO_3^{2-}, as illustrated in Figs. 9(b) and 9(c). The diffused copper ions may deposit between individual nanowires, resulting in the connection and aggregation of the nanowires. These aggregated CuO nanowires could still provide a sufficient amount of the active species for the OER. This may be the reason why the current remained stable despite the morphological change. Finally, a new nanosheet morphology formed after 20 h of the stability test. This offers a novel methodology for the preparation of composites of nanosheets and nanowires from single-component nanowire templates. In conclusion, we have presented a facile and low-cost method for the synthesis of a highly efficient electrode for the OER using crystalline CuO as the active species, and explored the origin of the high efficiency and long-term stability.

4 Conclusions

The OER activities of $Cu(OH)_2$, Cu_2O, CuO_x, and CuO with varied degrees of crystallization were investigated experimentally. The nanowires composed of $Cu(OH)_2$ or Cu_2O showed poor activity towards the OER in water electrolysis. With improved crystallinity and the formation of CuO, the OER activity increased drastically. The A-180 sample showed the highest water splitting ability, the smallest Tafel slope of 41 mV/decade, and almost 100% faradaic efficiency, as a result of the large amount of the active species (i.e., crystalline CuO). After a 15-hour stability test, the chemical composition of the electrode remained unchanged, resulting in a stable current density over time. During the stable water electrolysis, especially after 10 h of testing, copper ions diffused from the interior to the surface of the nanowires, leading to a decrease in the density and an increase in the porosity of the nanowires.

Acknowledgements

The XRD and electron microscopy characterizations were conducted at the Advanced Characterization Nanotechnology Platform of the University of Tokyo, supported by "Nanotechnology Platform" of the Ministry of Education, Culture, Sports, Science and Technology (MEXT), Japan. Part of this work was supported by JSPS KAKENHI Grant Number (17H03229), the JSPS Core-to-Core program (Advanced Research Networks type A), Japan (JSPS)-Korea (NRF) Bilateral program and Grants-in-Aids for Specially Promoted Research. The authors thank Prof. Yuichi Ikuhara of the University of Tokyo for his helpful discussion on electron microscopy data. The authors also thank Prof. Kazunari Domen and Prof. Takashi Hisatomi for assistance in determination of the faradaic efficiency. J. Y. thanks the support from China Scholarship Council (No. 201506210091).

Electronic supplementary Material: Supplementary material (SEM images, CV curves, sample photos and Raman spectroscopy measurements) is available in the online version of this article at https://doi.org/10.1007/s12274-018-2020-1.

References

[1] Yu, J.; Si, Z. C.; Chen, L.; Wu, X. D.; Weng, D. Selective catalytic reduction of NO_x by ammonia over phosphate-containing $Ce_{0.75}Zr_{0.25}O_2$ solids. *Appl. Catal. B: Environ.* **2015**, *163*, 223–232.

[2] Mamaca, N.; Mayousse, E.; Arrii-Clacens, S.; Napporn, T. W.; Servat, K.; Guillet, N.; Kokoh, K. B. Electrochemical activity of ruthenium and iridium based catalysts for oxygen evolution reaction. *Appl. Catal. B: Environ.* **2012**, *111–112*, 376–380.

[3] da Silva, G. C.; Perini, N.; Ticianelli, E. A. Effect of temperature on the activities and stabilities of hydrothermally prepared IrO_x nanocatalyst layers for the oxygen evolution reaction. *Appl. Catal. B: Environ.* **2017**, *218*, 287–297.

[4] Heo, I.; Wiebenga, M. H.; Gaudet, J. R.; Nam, I. S.; Li, W.; Kim, C. H. Ultra low temperature CO and HC oxidation over Cu-based mixed oxides for future automotive applications. *Appl. Catal. B: Environ.* **2014**, *160–161*, 365–373.

[5] Ng, J. W. D.; García-Melchor, M.; Bajdich, M.; Chakthranont, P.; Kirk, C.; Vojvodic, A.; Jaramillo, T. F. Gold-supported cerium-doped NiO_x catalysts for water oxidation. *Nat. Energy* **2016**, *1*, 16053.

[6] Zhong, M.; Hisatomi, T.; Kuang, Y. B.; Zhao, J.; Liu, M.; Iwase, A.; Jia, Q. X.; Nishiyama, H.; Minegishi, T.; Nakabayashi, M. et al. Surface modification of CoO_x loaded $BiVO_4$ photoanodes with ultrathin p-type NiO layers for improved solar water oxidation. *J. Am. Chem. Soc.* **2015**, *137*, 5053–5060.

[7] Cao, Q.; Yu, J.; Yuan, K. P.; Zhong, M.; Delaunay, J. J. Facile and large-area preparation of porous Ag_3PO_4 photoanodes for enhanced photoelectrochemical water oxidation. *ACS Appl. Mater. Interfaces* **2017**, *9*, 19507–19512.

[8] McCrory, C. C. L.; Jung, S.; Peters, J. C.; Jaramillo, T. F. Benchmarking heterogeneous electrocatalysts for the oxygen evolution reaction. *J. Am. Chem. Soc.* **2013**, *135*, 16977–16987.

[9] Feng, J. X.; Ye, S. H.; Xu, H.; Tong, Y. X.; Li, G. R. Design and synthesis of FeOOH/CeO_2 heterolayered nanotube electrocatalysts for the oxygen evolution reaction. *Adv. Mater.* **2016**, *28*, 4698–4703.

[10] Du, J. L.; Chen, Z. F.; Ye, S. R.; Wiley, B. J.; Meyer, T. J. Copper as a robust and transparent electrocatalyst for water oxidation. *Angew. Chem., Int. Ed.* **2015**, *54*, 2073–2080.

[11] Zhong, M.; Hisatomi, T.; Sasaki, Y.; Suzuki, S.; Teshima, K.; Nakabayashi, M.; Shibata, N.; Nishiyama, H.; Katayama, M.; Yamada, T. et al. Highly active GaN-stabilized Ta_3N_5 thin-film photoanode for solar water oxidation. *Angew. Chem., Int. Ed.* **2017**, *56*, 4739–4743.

[12] Peng, X.; Wang, L.; Hu, L. S.; Li, Y.; Gao, B.; Song, H.; Huang, C.; Zhang, X. M.; Fu, J. J.; Huo, K. F. et al. *In situ* segregation of cobalt nanoparticles on VN nanosheets via nitriding of $Co_2V_2O_7$ nanosheets as efficient oxygen evolution reaction electrocatalysts. *Nano Energy* **2017**, *34*, 1–7.

[13] Chen, H. X.; Zhang, Q. B.; Han, X.; Cai, J. J.; Liu, M. L.; Yang, Y.; Zhang, K. L. 3D hierarchically porous zinc–nickel–cobalt oxide nanosheets grown on Ni foam as binder-free electrodes for electrochemical energy storage. *J. Mater. Chem. A* **2015**, *3*, 24022–24032.

[14] Lu, X. F.; Liao, P. Q.; Wang, J. W.; Wu, J. X.; Chen, X. W.; He, C. T.; Zhang, J. P.; Li, G. R.; Chen, X. M. An alkaline-stable, metal hydroxide mimicking metal-organic framework for efficient electrocatalytic oxygen evolution. *J. Am. Chem. Soc.* **2016**, *138*, 8336–8339.

[15] Feng, J. X.; Xu, H.; Dong, Y. T.; Ye, S. H.; Tong, Y. X.; Li, G. R. FeOOH/Co/FeOOH hybrid nanotube arrays as high-performance electrocatalysts for the oxygen evolution reaction. *Angew. Chem., Int. Ed.* **2016**, *55*, 3694–3698.

[16] Lu, X. F.; Gu, L. F.; Wang, J. W.; Wu, J. X.; Liao, P. Q.; Li, G. R. Bimetal-organic framework derived $CoFe_2O_4$/C porous hybrid nanorod arrays as high-performance electrocatalysts for oxygen evolution reaction. *Adv. Mater.* **2017**, *29*, 1604437.

[17] Wang, H. Y.; Hsu, Y. Y.; Chen, R.; Chan, T. S.; Chen, H. M.; Liu, B. Ni^{3+}-induced formation of active NiOOH on the spinel Ni-Co oxide surface for efficient oxygen evolution reaction. *Adv. Mater.* **2015**, *5*, 1500091.

[18] Li, S. W.; Wang, Y. C.; Peng, S. J.; Zhang, L. J.; Al-Enizi, A. M.; Zhang, H.; Sun, X. H.; Zheng, G. F. Co–Ni-based nanotubes/nanosheets as efficient water splitting electrocatalysts. *Adv. Energy Mater.* **2016**, *6*, 1501661.

[19] Zhan, T. R.; Liu, X. L.; Lu, S. S.; Hou, W. G. Nitrogen doped NiFe layered double hydroxide/reduced graphene oxide mesoporous nanosphere as an effective bifunctional electrocatalyst for oxygen reduction and evolution reactions. *Appl. Catal. B: Environ.* **2017**, *205*, 551–558.

[20] Li, L. L.; Zhang, L.; Ma, K. L.; Zou, W. X.; Cao, Y.; Xiong, Y.; Tang, C. J.; Dong, L. Ultra-low loading of copper modified TiO_2/CeO_2 catalysts for low-temperature selective catalytic reduction of NO by NH_3. *Appl. Catal. B: Environ.* **2017**, *207*, 366–375.

[21] Xu, W.; Lan, R.; Du, D. W.; Humphreys, J.; Walker, M.; Wu, Z. C.; Wang, H. T.; Tao, S. W. Directly growing hierarchical nickel-copper hydroxide nanowires on carbon fibre cloth for efficient electrooxidation of ammonia. *Appl. Catal. B: Environ.* **2017**, *218*, 470–479.

[22] Berenguer, R.; La Rosa-Toro, A.; Quijada, C.; Morallón, E.

Electrocatalytic oxidation of cyanide on copper-doped cobalt oxide electrodes. *Appl. Catal. B: Environ.* **2017**, *207*, 286–296.

[23] Cao, Q.; Che, R. C.; Chen, N. Scalable synthesis of Cu_2S double-superlattice nanoparticle systems with enhanced UV/visible-light-driven photocatalytic activity. *Appl. Catal. B: Environ.* **2015**, *162*, 187–195.

[24] Ye, Z.; Giraudon, J. M.; Nuns, N.; Simon, P.; De Geyter, N.; Morent, R.; Lamonier, J. F. Influence of the preparation method on the activity of copper-manganese oxides for toluene total oxidation. *Appl. Catal. B: Environ.* **2018**, *223*, 154–166

[25] Liu, X. M.; Sui, Y. M.; Yang, X. Y.; Wei, Y. J.; Zou, B. Cu nanowires with clean surfaces: Synthesis and enhanced electrocatalytic activity. *ACS Appl. Mater. Interfaces* **2016**, *8*, 26886–26894.

[26] Wang, G. X.; Sui, Y. M.; Zhang, M. N.; Xu, M.; Zeng, Q. X.; Liu, C.; Liu, X. M.; Du, F.; Zou, B. One-pot synthesis of uniform Cu_2O–CuO–TiO_2 hollow nanocages with highly stable lithium storage properties. *J. Mater. Chem. A* **2017**, *5*, 18577–18584.

[27] Paracchino, A.; Mathews, N.; Hisatomi, T.; Stefik, M.; Tilley, S. D.; Grätzel, M. Ultrathin films on copper(I) oxide water splitting photocathodes: A study on performance and stability. *Energy Environ. Sci.* **2012**, *5*, 8673–8681.

[28] Luo, J. S.; Steier, L.; Son, M. K.; Schreier, M.; Mayer, M. T.; Grätzel, M. Cu_2O nanowire photocathodes for efficient and durable solar water splitting. *Nano Lett.* **2016**, *16*, 1848–1857.

[29] Li, C. L.; Hisatomi, T.; Watanabe, O.; Nakabayashi, M.; Shibata, N.; Domen, K.; Delaunay, J. J. Positive onset potential and stability of Cu_2O-based photocathodes in water splitting by atomic layer deposition of a Ga_2O_3 buffer layer. *Energy Environ. Sci.* **2015**, *8*, 1493–1500.

[30] Barnett, S. M.; Goldberg, K. I.; Mayer, J. M. A soluble copper–bipyridine water-oxidation electrocatalyst. *Nat. Chem.* **2012**, *4*, 498–502.

[31] Chen, Z. F.; Meyer, T. J. Copper(II) catalysis of water oxidation. *Angew. Chem., Int. Ed.* **2013**, *52*, 700–703.

[32] Yu, F. S.; Li, F.; Zhang, B. B.; Li, H.; Sun, L. C. Efficient electrocatalytic water oxidation by a copper oxide thin film in borate buffer. *ACS Catal.* **2015**, *5*, 627–630.

[33] Hou, C. C.; Fu, W. F.; Chen, Y. Self-supported Cu-based nanowire arrays as noble-metal-free electrocatalysts for oxygen evolution. *ChemSusChem* **2016**, *9*, 2069–2073.

[34] Zhang, W.; Wen, X.; Yang, S.; Berta, Y.; Wang, Z. L. Single-crystalline scroll-type nanotube arrays of copper hydroxide synthesized at room temperature. *Adv. Mater.* **2003**, *15*, 822–825.

[35] Reichardt, W.; Gompf, F.; Aïn, M.; Wanklyn, B. M. Lattice dynamics of cupric oxide. *Z. Phys. B Condens. Matter* **1990**, *81*, 19–24.

[36] Xu, J. F.; Ji, W.; Shen, Z. X.; Li, W. S.; Tang, S. H.; Ye, X. R.; Jia, D. Z.; Xin, X. Q. Raman spectra of CuO nanocrystals. *J. Raman Spectrosc.* **1999**, *30*, 413–415.

[37] Deng, Y. L.; Handoko, A. D.; Du, Y. H.; Xi, S. B.; Yeo, B. S. *In situ* Raman spectroscopy of copper and copper oxide surfaces during electrochemical oxygen evolution reaction: Identification of Cu^{III} oxides as catalytically active species. *ACS Catal.* **2016**, *6*, 2473–2481.

[38] Reydellet, J.; Balkanski, M.; Trivich, D. Light scattering and infrared absorption in cuprous oxide. *Phys. Status Solidi (B)* **1972**, *52*, 175–185.

[39] Moulder, J. F.; Stickle, W. F.; Sobol, P. E.; Bomben, K. D. *Handbook of X-Ray Photoelectron Spectroscopy: A Reference Book of Standard Spectra for Identification and Interpretation of XPS Data*; Eden Prairie, MN: Physical Electronics, 1995.

[40] Li, C. L.; Li, Y. B.; Delaunay, J. J. A novel method to synthesize highly photoactive Cu_2O microcrystalline films for use in photoelectrochemical cells. *ACS Appl. Mater. Interfaces* **2014**, *6*, 480–486.

[41] Tahir, M.; Pan, L.; Idrees, F.; Zhang, X. W.; Wang, L.; Zou, J. J.; Wang, Z. L. Electrocatalytic oxygen evolution reaction for energy conversion and storage: A comprehensive review. *Nano Energy* **2017**, *37*, 136–157.

[42] Pickrahn, K. L.; Park, S. W.; Gorlin, Y.; Lee, H. B. R.; Jaramillo, T. F.; Bent, S. F. Active MnO_x electrocatalysts prepared by atomic layer deposition for oxygen evolution and oxygen reduction reactions. *Adv. Energy Mater.* **2012**, *2*, 1269–1277.

[43] Mao, S.; Lu, G. H.; Chen, J. H. Three-dimensional graphene-based composites for energy applications. *Nanoscale* **2015**, *7*, 6924–6943.

[44] Brooker, M. H.; Bates, J. B. Raman and infrared spectral studies of anhydrous Li_2CO_3 and Na_2CO_3. *J. Chem. Phys.* **1971**, *54*, 4788–4796.

[45] Su, D. W.; Xie, X. Q.; Dou, S. X.; Wang, G. X. CuO single crystal with exposed {001} facets-A highly efficient material for gas sensing and Li-ion battery applications. *Sci. Rep.* **2014**, *4*, 5753.

[46] Trasatti, S.; Petrii, O. A. Real surface area measurements in electrochemistry. *Pure Appl. Chem.* **1991**, *63*, 711–734.